Materials Advances

ROYAL SOCIETY OF CHEMISTRY

PAPER

View Article Online
View Journal

Cite this: DOI: 10.1039/d5ma01523e

Phosphorous acid-mediated novel synthesis of $MnPO_4{\cdot}H_2O$ and $Mn_2P_2O_7$ with a unique flower-like morphology: a new approach to manganese phosphate supercapacitors

Prakash Bobde,[ab] Kajal Uphade,[c] Sharath Kandambeth,[c] Shikha Wadhwa[d] and Ranjit Kumar *[e]

Received 28th December 2025,
Accepted 22nd April 2026

DOI: 10.1039/d5ma01523e

rsc.li/materials-advances

Manganese phosphates in various forms have garnered substantial interest because of their applications in energy storage, catalysis, and materials science. In this study, we present a novel phosphorous acid (H_3PO_3)-mediated approach for the facile synthesis of $MnPO_4{\cdot}H_2O$ and $Mn_2P_2O_7$ with a unique flower-like morphology. As precursors, $KMnO_4$ and H_3PO_3 were chosen to hydrothermally synthesize $MnPO_4{\cdot}H_2O$. The crystalline $Mn_2P_2O_7$ was produced by heating $MnPO_4{\cdot}H_2O$ for two hours at 700 °C. XRD, FTIR, FESEM, TEM, and other techniques were used to characterize the materials. The monoclinic structure of $MnPO_4{\cdot}H_2O$ and $Mn_2P_2O_7$ was confirmed by XRD. A possible formation mechanism is proposed, highlighting the role of H_3PO_3 as both a phosphorus source and a structure-directing agent. The electrochemical study showed that $Mn_2P_2O_7$ has a specific capacitance of 169 F g^{-1}, whereas that of $MnPO_4{\cdot}H_2O$ is 63 F g^{-1} at a current density of 1 A g^{-1}. This approach provides a straightforward, economical, and scalable pathway to manganese phosphates with a unique morphology, paving the way for a potential future material with enhanced performance in electrochemical and catalytic applications.

1. Introduction

Manganese phosphates, encompassing compounds such as $MnPO_4{\cdot}H_2O$ and $Mn_2P_2O_7$, represent a versatile class of materials that have gained substantial attention recently for their promising roles in energy storage systems, catalytic processes, and advanced materials engineering.[1] Transition metal phosphate materials exhibit intriguing characteristics due to their extensive use in electric, magnetic, dielectric, ceramic, laser host, and catalytic procedures.[2,3] A large number of studies have documented the ion exchange properties of transition metal phosphates.[3–5] Transition metal phosphates are extensively used as adsorbents, ionic conductors, catalysts, ion exchangers, catalyst carriers and catalysts due to their diverse structures.[6] These materials have found applications in supercapacitors, magnetic materials, heat resistant materials, friction materials, and molecular recognition, because of their exceptional physical and chemical characteristics.[7] As a result, transition metal phosphates have recently gained popularity as a materials science research area.[4,8,9]

The phosphate block unit is used to separate the metal phosphate compounds into PO_4^{3-}, HPO_4^{2-}, $H_2PO_4^{-}$, $P_2O_7^{4-}$, and $P_4O_{12}^{4-}$ units.[1] Metal(III) phosphates are generally insoluble in water and commonly occur in amorphous, crystalline, or partially crystalline forms. These metal phosphates have varying levels of crystallinity and pH-dependent surface charge characteristics.[6] The use of $MnPO_4{\cdot}H_2O$ as a functional material, such as a cathode material for lithium-ion batteries, is made easier by manganese's various oxidation states.[6,8,10] Notably, the morphology of these phosphates plays a critical role in enhancing their performance; hierarchical structures, such as flower-like architectures, offer increased surface area, improved ion diffusion pathways, and better electrochemical accessibility compared to bulk forms. It is crucial to look for a low-cost, straightforward synthesis approach for the bulk production of $MnPO_4{\cdot}H_2O$ to increase its use.[6,8,11–13] Christensen *et al.*[14] initially prepared $MnPO_4{\cdot}H_2O$ by combining manganese(III) nitrate with phosphoric acid and nitric acid, as well as by oxidizing manganese(II) nitrate with phosphoric acid. Other

[a] *Techknowgreen Research Laboratory-9, Building G A-4, 3rd Floor, Waters Square, New DP Road, Pimpri-Chinchwad, Pune, 411027, India*
[b] *Department of Research & Development, UPES University, Energy Acres Building, Bidholi, Dehradun, 248007, Uttarakhand, India*
[c] *Department of Chemistry, Shiv Nadar Institution of Eminence, Delhi-NCR, 201314, India*
[d] *Applied Science Cluster, School of Engineering, UPES University, Energy Acres Building, Bidholi, Dehradun, 248007, Uttarakhand, India*
[e] *Center for Advanced Materials, Department of Chemical Engineering, Shiv Nadar Institution of Eminence, Delhi-NCR, 201314, India.*
E-mail: ranjit.kumar@snu.edu.in

researchers used manganese(II) carbonate as a source and oxidized it by the action of nitric acid and phosphoric acid as part of an additional preparation technique.[15–17] Zhang *et al.* used $Mn(NO_3)_2$ with H_3PO_4 to synthesize hydrothermally controlled $MnPO_4{\cdot}H_2O$, at 130 °C in 16 h.[18] Hu *et al.* synthesized microporous manganese phosphate using organophosphonic acid from bulk manganese oxide *via* a soft templating method.[19] These previously documented techniques involved the evolution of harmful gases, including NO_2 and CO_2, and were time-consuming at high temperatures.[20]

The precipitation, sol–gel, and hydrothermal processes used to prepare manganese phosphate hydrate allowed for a close mixing of the solution's constituent elements, which facilitated quick homogenous nucleation, producing finer particles and higher-purity materials.[21–24] Mixed orthophosphates, like $LiMPO_4$ (where M can be Fe, Co, Ni, or Mn), provide good electrochemical performances in lithium-ion battery cathode materials and are another area of interest for solution-based approaches.[17,20–23] Manganese phosphate, when prepared using the typically high-temperature process and using concentrated acid (conc. HNO_3), causes particle aggregation and sintering, which improves its electrochemical performance.[20]

Many methods were used to prepare $MnPO_4{\cdot}H_2O$, and each had its own pros and cons. The precipitation procedure was often used to produce $MnPO_4{\cdot}H_2O$. This method involved mixing soluble manganese salts with phosphate sources in water. Although this method is easy to use and reasonably economical, it does not give precise control over crystal size, shape, and purity. The wide size range of the particles produced affects the material's properties and performance.[21–24]

Researchers have also used the sol–gel method, which involves breaking down and combining metal alkoxides or salts to create a sol. This sol is then converted to manganese phosphate monohydrate *via* gelation. While the sol–gel method allows for better control over the composition and consistency of the final product, it is often slow and requires high temperatures during the gelation process.[16,24,25] Researchers have studied microwave irradiation to encourage the nucleation and growth of cobalt manganese phosphate crystals.[26] This method reduces the time of synthesis and improves control over particle size. But it is important to carefully manage the synthesis conditions to prevent overheating and ensure consistent microwave energy distribution, as this could cause unwanted side effects.[26,27] The hydrothermal method was chosen for manganese phosphate monohydrate because it produces high-purity, well-defined crystals with better properties. Its scalability, energy efficiency, and eco-friendliness made it a good option for large-scale industrial production of $MnPO_4{\cdot}H_2O$.[28,29] In the hydrothermal synthesis method, the reaction takes place in a closed vessel under high temperatures and high pressures.[28,29]

For the synthesis of $MnPO_4{\cdot}H_2O$, similar challenges persisted despite using various synthesis techniques in the past. These challenges included complex or slow synthesis processes, difficulties in achieving high purity, trouble in controlling crystal size and shape, and the possible use of harmful chemicals or conditions in certain methods.[20,30] To overcome these limitations and boost the production of $MnPO_4{\cdot}H_2O$ with better properties for various applications, such as environmental clean-up, battery technology, and catalysis, scientists have previously explored various synthesis methods.[20,30] Furthermore, one-pot syntheses that integrate reduction and phosphorylation steps without additional oxidants or pH regulators are underrepresented, particularly for achieving hierarchical flower-like structures in a facile manner. Traditional reductive approaches often employ harsh agents, leading to byproduct formation and purification challenges, while morphology tuning typically demands multi-step processing or specialized precursors.

The present work introduces a phosphorous acid-mediated reductive pathway, which differs fundamentally in reaction chemistry from conventional phosphate-based methods that use Mn(II) or Mn(III) salts as precursors, and enables the formation of unique flower-like morphologies without external templating agents. Here we present hydrothermal synthesis of nanocrystalline $MnPO_4{\cdot}H_2O$ at 150 °C using only $KMnO_4$ and H_3PO_3 as precursors. In this approach, H_3PO_3 acts both as a reducing agent and a phosphate source, enabling a simple, rapid, low-cost, and eco-friendly one-pot process that avoids the use of additional manganese salts and does not release any harmful gases. Subsequent calcination at 700 °C conveniently converts $MnPO_4{\cdot}H_2O$ into $Mn_2P_2O_7$. To the best of our knowledge, this is the first reported synthesis of manganese phosphates *via* reduction with phosphorus acid (H_3PO_3). The simplicity of the process, combined with the high phase purity and unique morphology achieved, offers a significant advancement over conventional multi-reagent routes and provides an efficient pathway for producing these materials for potential applications in catalysis, supercapacitors, and battery materials.

2. Experimental

2.1. Materials and chemicals

$KMnO_4$ (AR grade) and H_3PO_3 (AR grade) were purchased from Fisher Scientific, India. The Teflon-lined stainless steel autoclave (250 mL) was purchased from Shilpa Enterprises, Nagpur, Maharashtra.

2.2. Synthesis

2.2.1. Synthesis of $MnPO_4{\cdot}H_2O$. In a beaker, 13.01 g (0.0822 M) $KMnO_4$ was dissolved in 150 mL of distilled water and stirred for 1 hour (solution A). In another beaker, 13.50 g (0.1644 M) H_3PO_3 was added to 50 mL of distilled water (solution B). The as-prepared solution B was slowly added to solution A under continuous stirring, and the pH of this solution was 1.1. The solution was further stirred for 2 hours under ambient conditions, and the pH of the solution changed to 1.5. The mixture was then hydrothermally treated at 150 °C for 16 hours in a Teflon-lined stainless steel autoclave, followed by filtration. The obtained product was washed multiple times with distilled water to neutralize any remaining acid. The

as-synthesized product was dried in an oven at 100 °C for 4 hours to obtain $MnPO_4{\cdot}H_2O$ nanoparticles.

2.2.2. Synthesis of $Mn_2P_2O_7$. The above prepared $MnPO_4{\cdot}H_2O$ was calcined in a muffle furnace at 700 °C for two hours in air to obtain $Mn_2P_2O_7$. Fig. 1 shows the schematic of the synthesis of $MnPO_4{\cdot}H_2O$ and $Mn_2P_2O_7$.

2.3. Characterization

$MnPO_4{\cdot}H_2O$ and $Mn_2P_2O_7$ were characterized using Fourier transform infrared (FTIR) spectroscopy (PerkinElmer Frontier FTIR). FTIR was used to identify the surface functional groups present in $MnPO_4{\cdot}H_2O$ and $Mn_2P_2O_7$. X-ray diffraction (XRD) (Bruker D8-Advance Eco) was utilized to analyze their crystalline structures. The surface morphology and structural features of $MnPO_4{\cdot}H_2O$ and $Mn_2P_2O_7$ were examined using a JEOL JSM-7600PLUS field emission scanning electron microscope (FE-SEM). High-resolution transmission electron microscopy (HRTEM) images were acquired using a JOEL JEM2100 HRTEM, and the images were obtained using an accelerating voltage of 300 kV. The thermal stability of the materials was studied using thermogravimetric analysis (TGA2 System, Mettler Toledo) under N_2 flow at a heating ramp of 10 °C per minute. The specific surface area was measured by the Brunauer–Emmett–Teller (BET) method using a Microtrac BELSORP MAX G instrument.

2.4. Electrochemical study

Electrochemical charge storage experiments were conducted using a Bio-Logic SP-50e potentiostat in a three-electrode configuration. The working electrode was fabricated by depositing the active material onto carbon paper (1 cm × 3 cm). For electrode preparation, 8 mg of $Mn_2P_2O_7$ or $MnPO_4{\cdot}4H_2O$ powder was dispersed with 1 mg of conductive carbon and 1 mg of Nafion binder in 1 mL of ethanol. Following 10 minutes of sonication, the homogeneous suspension was drop-cast onto the carbon paper substrate. The final deposited mass of the sample was 1 mg. Prior to electrochemical testing, the prepared electrodes were dried under an IR lamp. A graphite counter electrode and Hg–HgO reference electrode were utilized, with measurements conducted in 1.0 M KOH electrolyte at ambient temperature.

3. Results and discussion

3.1. Characterization

3.1.1. X-ray diffraction. The XRD pattern of the sample without hydrothermal treatment revealed an amorphous material without any characteristic peaks of manganese phosphate, as shown in Fig. 2(a). The XRD patterns of the hydrothermally treated sample and the calcined sample are shown in Fig. 2(b and c). Lattice parameters of the synthesized samples were calculated from XRD data using MDI JADE 6.0 software by performing peak analysis, phase matching, and refinement. The peaks in Fig. 2(b) were matched with the $MnPO_4{\cdot}H_2O$ structure (JCPDS# 440071). These findings indicate that $MnPO_4{\cdot}H_2O$ possesses a monoclinic crystal structure with the space group $C2/c$. X-ray line broadening was used to calculate the average crystallite size. The average crystallite size for $MnPO_4{\cdot}H_2O$ was 56.17 nm, calculated from Scherrer's formula (*i.e.* $D = 0.89\lambda/\beta\cos\theta$), where λ is the wavelength of Cu-K_α radiation, D is 0.89 (constant), θ is the diffraction angle, and β is the full width at half maximum (FWHM).[20] The reflections at 2θ values 18.2(110), 19.1($11\bar{1}$), 23.8 (020), 25.3(111), 27.2($11\bar{2}$), 30.2($20\bar{2}$), 35.6(022), 41.0($31\bar{1}$), 42.9(221), 47.6($31\bar{3}$) and 56.2($22\bar{4}$) match perfectly with the peaks of $MnPO_4{\cdot}H_2O$. The lattice parameters of $MnPO_4{\cdot}H_2O$ closely match those reported in the standard reference JCPDS# 440071. The peaks in Fig. 2(c) at 2θ values 17.1($\bar{1}10$), 20.0(001), 28.7(111), 28.9(021), 30.4($\bar{2}01$), 34.7($\bar{2}20$), 41.6(131), 43.5(221), 49.2($\bar{2}22$), and 56.9 (400) were matched with the $Mn_2P_2O_7$ (JCPDS# 290891). These results indicate that $Mn_2P_2O_7$ exhibits a monoclinic crystal structure with the space group $C2/m$. The average crystallite size of 30.82 nm for the $Mn_2P_2O_7$ sample was calculated using the Scherrer equation.[20] The lattice parameters of $Mn_2P_2O_7$ match those of the standard data (JCPDS# 290891). The XRD data confirm the phase purity of the synthesized material (Table 1).

3.1.2. FTIR. The FTIR spectrum (Fig. 3) provides additional evidence for the generation of the $MnPO_4{\cdot}H_2O$ structure. The

Fig. 1 Schematic illustration of the synthesis of $MnPO_4{\cdot}H_2O$ and $Mn_2P_2O_7$.

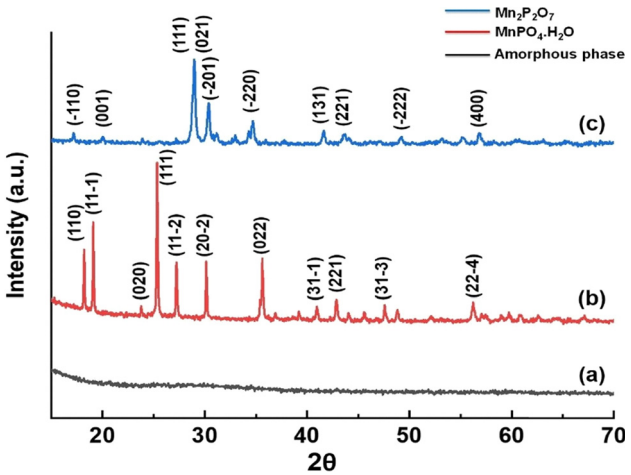

Fig. 2 (a) Amorphous manganese phosphate, (b) $MnPO_4{\cdot}H_2O$ and (c) $Mn_2P_2O_7$ XRD patterns.

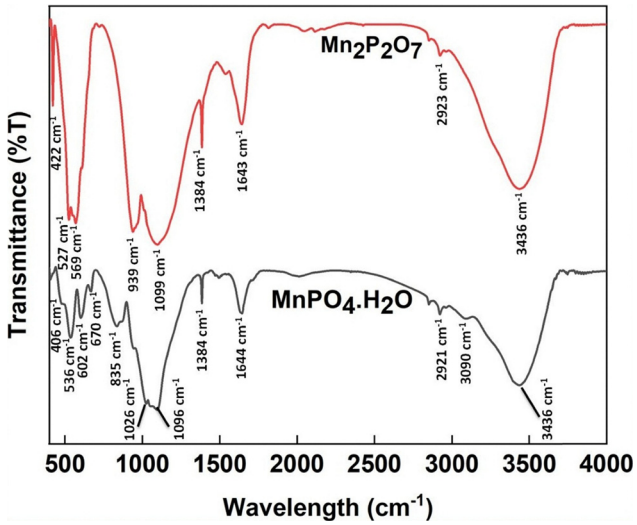

Fig. 3 FTIR spectra of $MnPO_4{\cdot}H_2O$ and $Mn_2P_2O_7$.

fundamental vibrating units, PO_4^{3-} ions and H_2O molecules, are used to identify the FTIR bands. The water bending and stretching vibrations are responsible for the bands that were seen at about 1644 and 3436 cm^{-1}, respectively.[17] Three bands show up in the hydroxyl stretching (3436, 3090, and 2921 cm^{-1}).[17] P–OH stretching is responsible for the primary absorption band, which is centered at 3090 cm^{-1} and characteristic of hydrogen phosphates.[31] On the other hand, it is also conceivable that the overtones $\upsilon_2(H_2O)$ and $\upsilon_1(H_2O)$ are assigned to the potential Fermi resonance.[32] The band at 1384 cm^{-1} was observed due to the residual phosphite group, which originates from the incomplete oxidation of H_3PO_3. The band in the region 1300–1400 cm^{-1} was due to the P–H bending and P–O stretching vibrations of phosphite ions.[33] The other two bands at 3436 and 2921 cm^{-1} appear as shoulders. When the water interacts effectively through the hydrogen bonds, the first band is attributed to υ(H–O–H). It is possible to attribute the second shoulder to υ(MnO–H), $\upsilon(H_3O^+)$, or both.[17,31] The doubly degenerate band at 1096 cm^{-1} and non-degenerate band at 1026 cm^{-1} appeared due to the splitting of the solitary PO_4^{3-} tetrahedron's triply degenerate asymmetric stretching vibrations into two bands. The peaks at approximately 835, 670, 602, 536, and 406 cm^{-1} wavenumbers were due to vibrations of υ(P–OH) stretching, δ(Mn–O–H) bending, δ(P–O–Mn), $\upsilon 4(PO_4^{3-})$, and υ(Mn–OP), respectively.[17] The two peaks at 835 and 670 cm^{-1} disappeared in $Mn_2P_2O_7$ due to the calcination at high temperature of $MnPO_4{\cdot}H_2O$.[17] The characterization and analysis presented above confirm the characteristic vibrations of $MnPO_4{\cdot}H_2O$.

The FTIR spectra of $Mn_2P_2O_7$ shown in Fig. 3 indicate the fundamental vibrations of the $P_2O_7^{4-}$ anion. Among the spectrum's most notable characteristics are the strong bands located at 1099, 939, 569, 527, and 422 cm^{-1}. υ_{as} (PO_3), υ_{as} (P–O–P), δ (PO_3), δ (PO_3), and ρ (PO_3) can all be attributed to these bands.[1] The symmetric and asymmetric stretching vibrations of the P–O–P bridge (υ_{as} POP and υ_s POP) observed in the 700–970 cm^{-1} range confirm $P_2O_7^{4-}$ anions with bent P–O–P angles.[1] Comparing the two spectra, it can be clearly seen that the peaks at 835 and 602 cm^{-1} in $MnPO_4{\cdot}H_2O$ disappear completely in $Mn_2P_2O_7$.[17] These two peaks are assigned to the stretching vibrations of P–OH and the bending vibration of Mn–O–H, respectively, which disappear after calcination when the structure is converted to $Mn_2P_2O_7$.[1,17]

3.1.3. SEM. The SEM images show the flower-like morphology of $MnPO_4{\cdot}H_2O$ and $Mn_2P_2O_7$ (Fig. 4). $MnPO_4{\cdot}H_2O$ exhibited uniform polycrystals, consisting of nanoparticles with a size distribution ranging from small particles (200–400 nm) to larger ones (>400–600 nm). This morphology suggests the presence of nucleation sites that lead to nanocrystal growth during hydrothermal treatment, although the exact mechanisms remain unclear. $Mn_2P_2O_7$ displays a porous structure with agglomerated small particles measuring 80–100 nm. The porous surface structure observed on the particles likely results from the decomposition process.

Table 1 Average crystallite sizes and structural parameters of $MnPO_4{\cdot}H_2O$ and $Mn_2P_2O_7$ calculated from the XRD data

	$MnPO_4{\cdot}H_2O$			$Mn_2P_2O_7$		
Lattice parameters	This work	PDF#440071	Difference (this work-PDF)	This work	PDF#290891	Difference (this work-PDF)
a (Å)	6.947	6.928	0.019	6.657	6.636	0.021
b (Å)	7.483	7.478	0.005	8.592	8.584	0.008
c (Å)	7.386	7.372	0.014	4.540	4.545	−0.005
β (°)	112.28	112.30	−0.020	102.86	102.78	0.080
Average crystallite size	56.17 nm			30.82 nm		

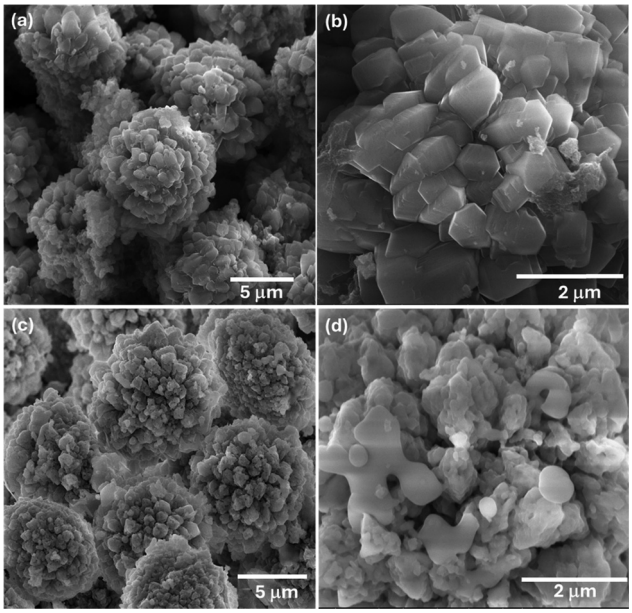

Fig. 4 SEM micrographs of (a and b) $MnPO_4{\cdot}H_2O$ and (c and d) $Mn_2P_2O_7$.

3.1.4. TEM. The TEM micrograph of $MnPO_4{\cdot}H_2O$, as shown in Fig. 5(a and b), confirms the nanorod-like structure of the particle. The crystalline nature of the as-synthesized $MnPO_4{\cdot}H_2O$ and the calcined $Mn_2P_2O_7$ was primarily confirmed by powder XRD, which showed sharp diffraction peaks indexed to the monoclinic phases. The SAED pattern of $Mn_2P_2O_7$ aligns well with the XRD data, which confirms its monoclinic crystal structure (space group $C2/m$). The key d-spacings include 3.08 Å (021), 2.94 Å ($\bar{2}01$), 2.58 Å (220), and 2.17 Å (131), which would produce rings at corresponding reciprocal distances. The observed pattern's ring distribution and spotty nature are consistent with nanocrystalline $Mn_2P_2O_7$, often seen in derivatives from thermal decomposition of precursors like manganese phosphates.[34]

In comparison, $MnPO_4{\cdot}H_2O$ has a distinct monoclinic structure (space group $C2/c$). Its prominent d-spacings are larger overall, such as 4.86 Å (110), 4.64 Å ($11\bar{1}$), 3.51 Å (111), 3.32 Å ($11\bar{2}$), 2.95 Å ($20\bar{2}$), and 2.52 Å (022). An SAED pattern for $MnPO_4{\cdot}H_2O$ would thus feature inner rings at smaller reciprocal distances (larger d-values) compared to $Mn_2P_2O_7$, reflecting its different unit cell and bonding (orthophosphate PO_4^{3-} groups with coordinated water *vs.* pyrophosphate $P_2O_7^{4-}$ in $Mn_2P_2O_7$).

3.1.5. Thermogravimetric analysis. Thermogravimetric analysis (TGA) of $MnPO_4{\cdot}H_2O$ and $Mn_2P_2O_7$ reveals distinct thermal decomposition stages, as shown in Fig. 6. The TGA graph of $MnPO_4{\cdot}H_2O$ indicates an initial weight loss of approximately 6% from 100 °C to 320 °C, primarily attributed to the dehydration of the monohydrate, where the coordinated water molecule is released, forming anhydrous $MnPO_4$. A subsequent, more significant weight loss of 18% occurs between 320 °C and 510 °C, likely due to the decomposition of the phosphate structure, possibly involving the release of volatile components or structural rearrangement, reducing the sample to 84 wt%.[13] Beyond 510 °C, the weight stabilizes at approximately 83%, indicating the formation of a thermally stable phase of $Mn_2P_2O_7$, with no further significant mass loss. The TGA graph of $Mn_2P_2O_7$ shows no significant weight loss until 900 °C, indicating a thermally stable material.

3.1.6. BET surface area. The surface area of manganese pyrophosphate ($Mn_2P_2O_7$) and manganese phosphate monohydrate ($MnPO_4{\cdot}H_2O$) was determined using the Brunauer–Emmett–Teller (BET) method. $Mn_2P_2O_7$ showed a typical type IV isotherm, whereas $MnPO_4{\cdot}H_2O$ showed an open hysteresis loop due to slow kinetics in the micropores or structural changes. $Mn_2P_2O_7$ exhibited a moderate BET surface area of 25.0 $m^2\ g^{-1}$, indicating a reasonably porous structure suitable for applications requiring good accessibility of the active sites. In contrast, $MnPO_4{\cdot}H_2O$ showed a significantly lower BET surface area of 8.1 $m^2\ g^{-1}$, suggesting a more compact or less porous morphology with reduced external surface available for interaction. These differences in surface area between the two manganese phosphate compounds can influence their performance in catalytic, electrochemical, or adsorption-related processes (Fig. 7).

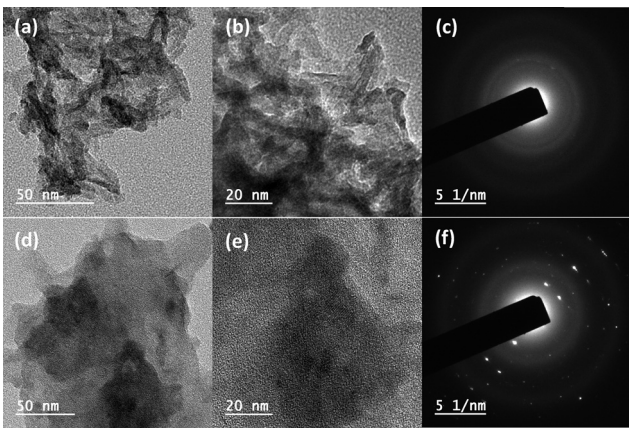

Fig. 5 TEM micrographs of $MnPO_4{\cdot}H_2O$ (a) and (b) and $Mn_2P_2O_7$ (d) and (e), and SAED patterns of (c) $MnPO_4{\cdot}H_2O$ and (f) $Mn_2P_2O_7$.

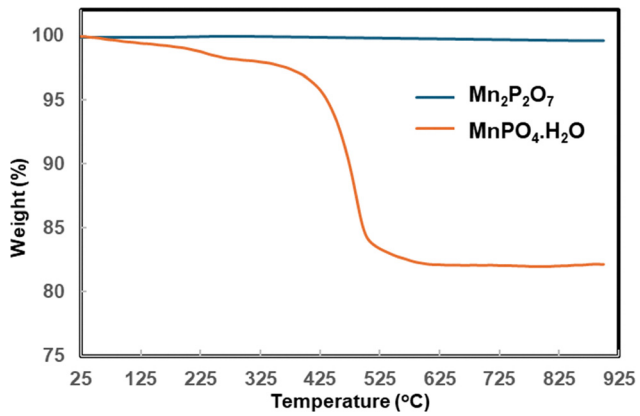

Fig. 6 TGA plot of $MnPO_4{\cdot}H_2O$ and $Mn_2P_2O_7$.

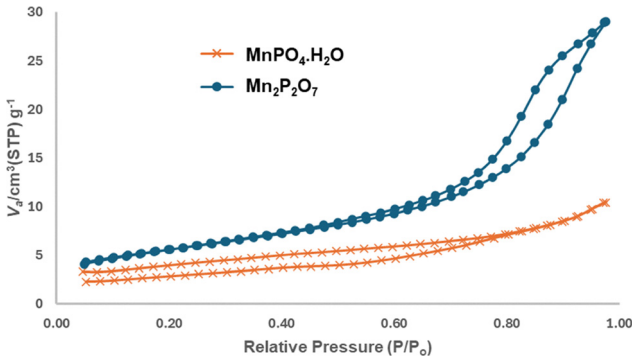

Fig. 7 BET N_2 adsorption isotherm of $MnPO_4{\cdot}H_2O$ and $Mn_2P_2O_7$.

3.2. Plausible mechanism of $MnPO_4{\cdot}H_2O$ and $Mn_2P_2O_7$ formation

The synthesis of manganese phosphate monohydrate ($MnPO_4{\cdot}H_2O$) using phosphorous acid (H_3PO_3) and potassium permanganate ($KMnO_4$) as the sole manganese source involves a redox-driven precipitation reaction under controlled conditions. $KMnO_4$ is a strong oxidizing agent in aqueous solution, where it dissociates to form permanganate ions (MnO_4^-). The manganese in MnO_4^- is in the +7 oxidation state (Mn(VII)). In the presence of a reducing agent, MnO_4^- can be reduced to lower oxidation states, such as Mn(III), which is required for the formation of $MnPO_4{\cdot}H_2O$, where manganese exists as Mn^{3+}.[35] The progress of the reaction was monitored by UV-vis spectroscopy (Fig. S1) and the colour change of the solution. The colour of the solution changed from purple (Mn^{7+}) to brown pink (Mn^{3+}), which was also indicated by the decrease in absorbance of typical peaks of MnO_4^- species (490–570 nm) as H_3PO_3 was added to the $KMnO_4$ solution. Possibly, some Mn^{2+} also forms transiently or as an intermediate during the initial reduction step. However, the hydrothermal treatment oxidises any remaining Mn^{2+} phase (or dissolved Mn^{2+}) to the Mn^{3+} product, because of the presence of MnO_4^-.

Phosphorous acid (H_3PO_3) serves a dual purpose. First, it acts as a reducing agent, capable of reducing Mn(VII) in MnO_4^- to Mn(III). Second, upon oxidation, H_3PO_3 is converted to phosphate ions (PO_4^{3-}), which are essential for forming the $MnPO_4{\cdot}H_2O$ product. The oxidation of H_3PO_3 to H_3PO_4 (phosphoric acid) provides the phosphate groups necessary for the precipitation reaction. H_3PO_3 plays another significant role as a structure-directing agent. The presence of PO_3^{3-} ions in the solution helps in the development of a unique flower-like morphology as was evidenced in the FESEM images.[36,37]

Redox reaction: The synthesis begins with the redox reaction between MnO_4^- and H_3PO_3 (eqn (1)). In an acidic aqueous medium, the permanganate ion is reduced, and H_3PO_3 is oxidized. The simplified redox reaction can be represented as follows:

Reduction half-reaction:

$$MnO_4^- + 8H^+ + 4e^- \rightarrow Mn^{3+} + 4H_2O \quad (1)$$

Here, Mn(VII) is reduced to Mn(III).

Oxidation half-reaction:

$$H_3PO_3 + H_2O \rightarrow H_3PO_4 + 2H^+ + 2e^- \quad (2)$$

H_3PO_3 is oxidized to H_3PO_4, releasing phosphate ions (PO_4^{3-}) upon dissociation of H_3PO_4 in solution (eqn (2)).

The overall redox reaction can be written as

$$MnO_4^- + H_3PO_3 + 4H^+ \rightarrow Mn^{3+} + H_3PO_4 + 2H_2O \quad (3)$$

Formation of $MnPO_4{\cdot}H_2O$: once Mn^{3+} and PO_4^{3-} ions are generated in the solution, they combine to form the insoluble $MnPO_4{\cdot}H_2O$ precipitate (eqn (4)). The reaction can be written as:

$$Mn^{3+} + PO_4^{3-} + H_2O \rightarrow MnPO_4{\cdot}H_2O\ (s) \quad (4)$$

The monohydrate form incorporates one water molecule per formula unit, which is typical for manganese phosphate synthesized under aqueous conditions. The reaction conditions, such as pH, temperature, and concentration, are critical to ensure the formation of the monohydrate phase with high crystallinity and purity.

The synthesis typically occurs in an aqueous medium under mild conditions resulting in the formation of an amorphous manganese phosphate. Treatment of this amorphous manganese phosphate by the hydrothermal method at 150 °C results in a crystalline $MnPO_4{\cdot}H_2O$ phase as confirmed by X-ray diffraction analysis. The pH of the solution influences the dissociation of H_3PO_4 and the stability of the Mn^{3+} ions. An acidic (pH $\sim$ 1.5) environment is maintained to facilitate the redox reaction and prevent the formation of undesirable manganese oxides or hydroxides.

Upon heating to 700 °C, the anhydrous $MnPO_4$ undergoes a condensation reaction, where two orthophosphate units combine, releasing oxygen to form manganese pyrophosphate ($Mn_2P_2O_7$) (eqn (5)).[38] The reaction can be written as:

$$2MnPO_4 \rightarrow Mn_2P_2O_7 + \tfrac{1}{2}O_2 \quad (5)$$

$Mn_2P_2O_7$, which is a thermally stable pyrophosphate phase, consists of $P_2O_7^{4-}$ anions (pyrophosphate groups) coordinated with Mn^{2+} cations, forming a crystalline lattice. The transformation of $MnPO_4{\cdot}H_2O$ to $Mn_2P_2O_7$ upon calcining at 700 °C proceeds through dehydration to form $MnPO_4$, followed by thermal decomposition and condensation of the phosphate units, resulting in the stable pyrophosphate phase. The TGA data support this, with the observed weight losses aligning with the loss of water and structural reorganisation, resulting in the formation of $Mn_2P_2O_7$.

H_3PO_3's dual role as a reducing agent and phosphate source further streamlines the process, reducing the number of reagents and minimizing byproducts. The redox-driven mechanism enables precise control over the formation of $MnPO_4{\cdot}H_2O$, ensuring high phase purity with unique morphology. This synthesis method for $MnPO_4{\cdot}H_2O$ under appropriate aqueous conditions and subsequent calcination to produce $Mn_2P_2O_7$

offers an efficient route to this material for applications in catalysis, supercapacitors, battery materials, and other fields.

3.3. Electrochemical performance of $Mn_2P_2O_7$

To study the electrochemical properties of $Mn_2P_2O_7$ and $MnPO_4{\cdot}H_2O$, a three-electrode configuration was employed with 1 M KOH electrolyte, a reference electrode of Hg–HgO, and a counter electrode made of graphite. Cyclic voltammetry (CV) measurements of $Mn_2P_2O_7$ conducted at various scan rates revealed that the capacitance contribution predominantly occurs in the positive potential window (−0.04 V to 0.67 V *vs.* Hg–HgO), as shown in Fig. 8. The CV curve of $Mn_2P_2O_7$ at 5 mV s^{-1} exhibited two distinct redox peaks at approximately 0.38 V and 0.47 V (*vs.* Hg–HgO).

Similarly, $MnPO_4{\cdot}4H_2O$ displayed capacitive behaviour in the positive potential range (−0.26 V to 0.8 V) at 10 mV s^{-1} scan rate. The CV profile of $MnPO_4$ showed characteristic peaks at 0 V and 0.6 V. To further assess the charge storage capabilities of these materials, galvanostatic charge/discharge (GCD) measurements were performed by varying the current density from 1 to 20 A g^{-1}.

The following formula was used to calculate specific capacitance (C_s, F g^{-1}) from the GCD curves:

$$C_s = 2I\int V\mathrm{d}t/m(\Delta V)^2$$

where I represents the applied current (mA), m is the active material mass (g), $\int V\mathrm{d}t$ denotes the area under the discharge curve in a GCD, and ΔV is the potential window.

GCD analysis revealed that $Mn_2P_2O_7$ showed a specific capacitance value of 169 F g^{-1} at 1 A g^{-1} current density. Although the specific capacitance decreased upon increasing current density, $Mn_2P_2O_7$ still retained 40% of its initial specific capacitance value even at a high current density. In contrast, $MnPO_4$ exhibited a lower specific capacitance value of 63 F g^{-1} at 1 A g^{-1} and showed a drastic decrease in specific capacitance (5.5%) at higher current density (20 A g^{-1}), yielding only 3.5 F g^{-1}.[39]

When compared with $MnPO_4{\cdot}H_2O$, $Mn_2P_2O_7$ exhibits a markedly superior electrochemical performance. At a current density of 1 A g^{-1}, $Mn_2P_2O_7$ delivers a specific capacitance of 169 F g^{-1}, which is nearly 2.7 times higher than that of $MnPO_4{\cdot}H_2O$ (63 F g^{-1}). This significant enhancement can be attributed to the distinct phosphate framework and higher density of electrochemically active manganese sites in $Mn_2P_2O_7$, which facilitate more effective faradaic redox reactions (Mn^{2+}/Mn^{3+}). Additionally, the pyrophosphate structure is likely to provide improved structural robustness and better ion diffusion pathways compared to the hydrated orthophosphate phase, thereby contributing to enhanced charge-storage capability. The relatively lower capacitance of $MnPO_4{\cdot}H_2O$ may arise from its more compact crystal structure and the presence of coordinated water molecules, which can impede electron transport and limit the utilization of the active material. The electrochemical performance of $Mn_2P_2O_7$, with a specific capacitance of 169 F g^{-1} at a current density of 1 A g^{-1}, highlights its potential as a promising pseudocapacitive electrode material for supercapacitor applications. This moderate yet significant capacitance, achieved in a pure and unmodified form, reflects the intrinsic redox activity of manganese species and the reversible faradaic charge-storage mechanism of the phosphate

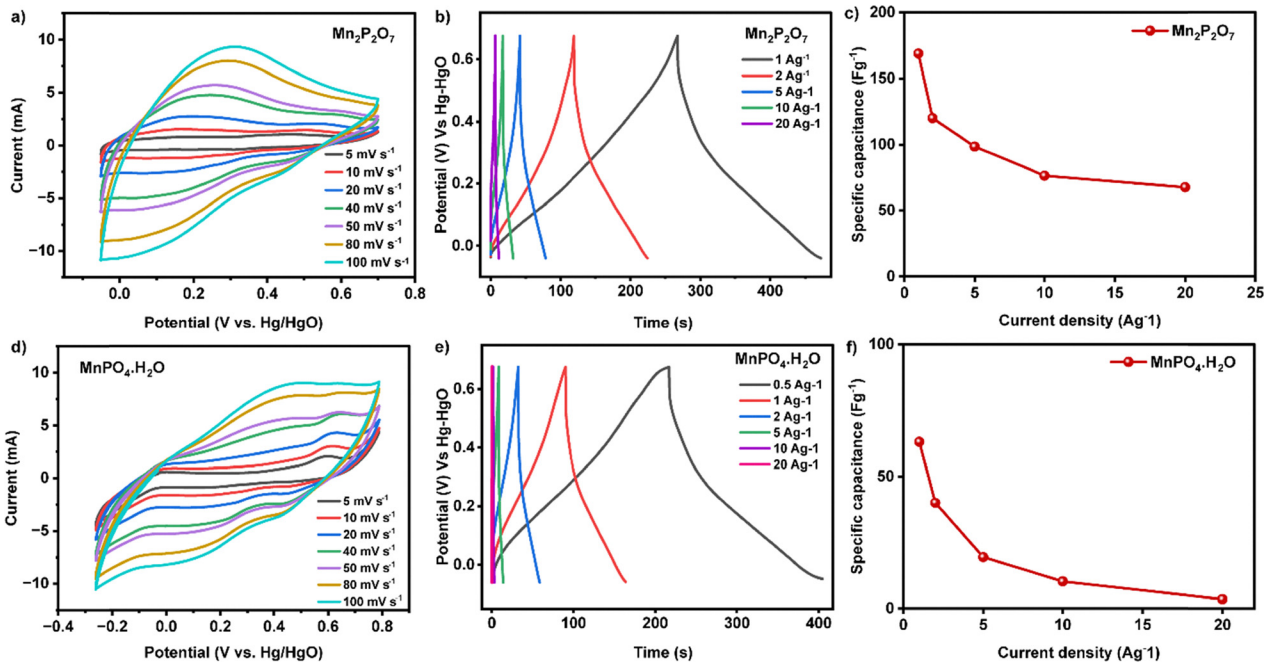

Fig. 8 (a) CV curves of $Mn_2P_2O_7$ at various scan rates, (b) GCD curves of $Mn_2P_2O_7$ at different current densities, (c) specific capacitances of $Mn_2P_2O_7$ *vs.* current density, (d) CV curves of $MnPO_4{\cdot}H_2O$ at various scan rates, (e) GCD curves of $MnPO_4{\cdot}H_2O$ at different current densities, and (f) specific capacitances of $MnPO_4{\cdot}H_2O$ *vs.* current density.

Table 2 Comparison of the specific capacitance of $Mn_2P_2O_7$ (and the composites) reported in recent literature

Material	Specific capacitance	Current density (A g^{-1})	Electrolyte (M KOH)	Electrode configuration	Ref.
Flower-like $Mn_2P_2O_7$	169 F g^{-1}	1	1	Drop-cast on carbon paper	This work
$Mn_2P_2O_7$ nanosheets (freeze-dried)	~140–180 F g^{-1}	1	3	Ni foam	40
$Mn_2P_2O_7$ nanoclusters	~120–160 F g^{-1}	1	1	Three electrode	41
$Mn_2P_2O_7$ (from Mn-organic phosphate, calcined at 550 °C)	230.9 F g^{-1}	0.5	3	Three electrode	39
$Mn_2P_2O_7$@polypyrrole (sunflower-like composite)	658 F g^{-1}	1	1	Ni foam	42
$Mn_2P_2O_7$ (in PANI hybrid study)	750 C g^{-1}	1	4	Three electrode	43

framework. Owing to its structural stability, earth abundance, and environmentally benign nature, $Mn_2P_2O_7$ is particularly attractive for cost-effective and sustainable energy storage systems. While the relatively low electrical conductivity of phosphate-based materials may limit its performance, $Mn_2P_2O_7$ can serve as an efficient base material for further performance enhancement through nanostructuring or hybridization with conductive matrices. Therefore, $Mn_2P_2O_7$ holds considerable potential for use in next-generation supercapacitors, especially in composite or asymmetric device configurations where improved power and energy densities are desired.[39]

$Mn_2P_2O_7$ exhibited excellent specific capacity retention (100%) over 250 cycles at a current density of 5 A g^{-1} as shown in Fig. S3. Cyclic voltammetry (CV) at varying scan rates (5 to 100 mV s^{-1}), was conducted within the selected potential window (0 V to 0.4 V), to calculate the electrochemically active surface area. The ECSA values are found to be 0.41 cm^2 for the $Mn_2P_2O_7$ sample.

BET surface area calculations showed that $Mn_2P_2O_7$ possessed a higher surface area (25.0 m^2 g^{-1}) than $MnPO_4{\cdot}H_2O$ (8.1 m^2 g^{-1}). Since capacitance directly correlates with the electrode surface area, $MnPO_4{\cdot}H_2O$'s limited surface area likely hindered its charge storage performance. This structural limitation explains why $MnPO_4{\cdot}H_2O$ exhibited substantially lower capacitance than $Mn_2P_2O_7$, particularly at higher charging rates, where efficient charge distribution becomes crucial.

Although the specific capacitance of our $Mn_2P_2O_7$ (169 F g^{-1} at 1 A g^{-1}) is lower than certain nanostructured or composite $Mn_2P_2O_7$ electrodes reported recently, it remains competitive among pure-phase materials synthesized *via* simple routes (Table 2). The performance gap relative to binder-free Ni-foam or polymer–composite electrodes is primarily attributed to differences in electrode configuration, conductivity, and mass loading. The flower-like morphology obtained through our H_3PO_3-mediated approach provides a good ion-accessible surface area while maintaining structural stability after calcination. Our future plans include making nanocomposites of $Mn_2P_2O_7$ with other conductive materials to improve the supercapacitor performance.

4. Conclusion

In conclusion, this study demonstrates a novel and efficient hydrothermal synthesis of $MnPO_4{\cdot}H_2O$ using $KMnO_4$ and H_3PO_3 as precursors, followed by thermal treatment at 700 °C for 2 hours to yield crystalline $Mn_2P_2O_7$. Unlike conventional methods that often require multiple manganese salts or complex phosphate sources, this approach streamlines the reaction by leveraging the strong oxidizing properties of $KMnO_4$ and the dual functionality of H_3PO_3. This reduces the number of reagents, minimizes byproducts, and enhances phase purity, as confirmed by XRD analysis showing pure monoclinic phases for both compounds. These findings contribute to the advancement of the synthesis methodologies for manganese-based materials, with potential applications in catalysis, energy storage, anti-corrosion coatings, *etc.*, paving the way for further exploration of tailored reaction conditions to optimize crystallite size and phase purity. $Mn_2P_2O_7$ demonstrated a specific capacitance of 169 F g^{-1} at 1 A g^{-1}, highlighting $Mn_2P_2O_7$ as a promising manganese phosphate-based electrode material and a viable platform for further optimization toward high performance supercapacitor applications.

Author contributions

Prakash Bobde: writing – review and editing, writing – original draft, validation, methodology, and investigation; Kajal Uphade: investigation; Sharath Kandambeth: investigation; Shikha Wadhwa: writing – review and editing, and resources; Ranjit Kumar: writing – review and editing, writing – original draft, resources, and conceptualisation.

Conflicts of interest

The authors declare that they have no known competing financial interests or personal relationships that could have appeared to influence the work reported in this paper.

Data availability

The authors declare that all the data supporting the findings of this study are available within the paper. Should any raw data files be needed in another format, they are available from the corresponding author upon reasonable request.

Supplementary information (SI) is available. See DOI: https://doi.org/10.1039/d5ma01523e.

Acknowledgements

We acknowledge the characterization facility at the Indian Institute of Petroleum, Dehradun, for FESEM and TEM

analysis. We would also like to thank the central characterization facility at UPES, Dehradun, for this study.

References

1 B. Boonchom, R. Baitahe, Z. Joungmunkong and N. Vittayakorn, Grass blade-like microparticle $MnPO_4{\cdot}H_2O$ prepared by a simple precipitation at room temperature, *Powder Technol.*, 2010, **203**(2), 310–314, DOI: 10.1016/J.POWTEC.2010.05.022.

2 H. Zhao and Z. Y. Yuan, Insights into Transition Metal Phosphate Materials for Efficient Electrocatalysis, *ChemCatChem*, 2020, 3797–3810, DOI: 10.1002/cctc.202000360.

3 S. Karafiludis, T. W. Ryll, A. G. Buzanich, F. Emmerling and T. M. Stawski, Phase stability studies on transition metal phosphates aided by an automated synthesis, *CrystEngComm*, 2023, **25**(30), 4333–4344, DOI: 10.1039/d3ce00386h.

4 G. Renaudin, S. Gomes and J. M. Nedelec, First-row transition metal doping in calcium phosphate bioceramics: A detailed crystallographic study, *Materials*, 2017, **10**(1), 92, DOI: 10.3390/ma10010092.

5 X. Li, X. Xiao, Q. Li, J. Wei, H. Xue and H. Pang, Metal (M = Co, Ni) phosphate based materials for high-performance supercapacitors, *Inorg. Chem. Front.*, 2018, **5**(1), 11–28, DOI: 10.1039/C7QI00434F.

6 G. Qiu, Z. Gao, H. Yin, X. Feng, W. Tan and F. Liu, Synthesis of $MnPO_4{\cdot}H_2O$ by refluxing process at atmospheric pressure, *Solid State Sci.*, 2010, **12**(5), 808–813, DOI: 10.1016/j.solidstatesciences.2010.02.014.

7 G. Tatrari, M. Karakoti, C. Tewari, S. Pandey, B. S. Bohra and A. Dandapat, *et al.*, Solid waste-derived carbon nanomaterials for supercapacitor applications: a recent overview, *Mater. Adv.*, 2021, **2**(5), 1454–1484, DOI: 10.1039/D0MA00871K.

8 N. Stegmann, C. Ochoa-Hernández, K. N. Truong, H. Petersen, C. Weidenthaler and W. Schmidt, The Mechanism and Pathway of Selective Partial Oxidation of n-Butane to Maleic Anhydride Studied on Titanium Phosphate Catalysts, *ACS Catal.*, 2023, **13**(24), 15833–15840, DOI: 10.1021/acscatal.3c03172.

9 C. Nithya, Transition Metal Phosphates/Phosphonates for Lithium-Ion Batteries, in *Engineering Materials*, 2023, pp. 283–299, DOI: 10.1007/978-3-031-27062-8_16.

10 T. Liu, C. Chen, S. Liu, Z. Chen, Z. Pu and Q. Huang, *et al.*, Transition metal phosphides as noble-metal-alternative cocatalysts for solar hydrogen production, *Coord. Chem. Rev.*, 2024, **521**, 216145, DOI: 10.1016/j.ccr.2024.216145.

11 N. L. W. Septiani, Y. V. Kaneti, K. B. Fathoni, K. Kani, A. E. Allah and B. Yuliarto, *et al.*, Self-assembly of two-dimensional bimetallic nickel-cobalt phosphate nanoplates into one-dimensional porous chainlike architecture for efficient oxygen evolution reaction, *Chem. Mater.*, 2020, **32**(16), 7005–7018, DOI: 10.1021/acs.chemmater.0c02385.

12 D. Zhang, L. L. Hu, Y. G. Sun, J. Y. Piao, X. S. Tao and Y. S. Xu, *et al.*, Construction of uniform transition-metal phosphate nanoshells and their potential for improving Li-ion battery performance, *J. Mater. Chem. A*, 2018, **6**(19), 8992–8999, DOI: 10.1039/c8ta01320a.

13 Y. Wang, G. Hu, Z. Peng, K. Du, B. Zhang and Y. Cao, Self-assembly synthesis of dumbbell-like $MnPO_4{\cdot}H_2O$ hierarchical particle and its application in $LiMnPO_4$/C cathode materials, *Ceram. Int.*, 2021, **47**(14), 19687–19693, DOI: 10.1016/J.CERAMINT.2021.03.306.

14 O. T. Christensen, Beiträge zur Kenntniss der Oxyde des Mangans, *J. Prakt. Chem.*, 1883, **28**(1), 1–37, DOI: 10.1002/PRAC.18830280101.

15 X. Bao, W. Bin Zhang, L. Zhang, Y. W. Guo, X. Zhou and X. L. Zhang, *et al.*, Alkali cation intercalation manganese phosphate hydrate boosting electrochemical kinetics for pseudocapacitive energy storage, *J. Materiomics*, 2022, **8**(4), 833–842, DOI: 10.1016/j.jmat.2022.01.005.

16 Y. Wang, G. Hu, Z. Peng, K. Du, B. Zhang and Y. Cao, Self-assembly synthesis of dumbbell-like $MnPO_4{\cdot}H_2O$ hierarchical particle and its application in $LiMnPO_4$/C cathode materials, *Ceram. Int.*, 2021, **47**(14), 19687–19693, DOI: 10.1016/j.ceramint.2021.03.306.

17 B. Boonchom, S. Youngme, S. Maensiri and C. Danvirutai, Nanocrystalline serrabrancaite ($MnPO_4{\cdot}H_2O$) prepared by a simple precipitation route at low temperature, *J. Alloys Compd.*, 2008, **454**(1–2), 78–82, DOI: 10.1016/J.JALLCOM.2006.12.064.

18 Y. Zhang, Y. Liu, S. Fu, F. Guo and Y. Qian, Hydrothermally Controlled Growth of $MnPO_4{\cdot}H_2O$ Single-Crystal Rods, *Bull. Chem. Soc. Jpn.*, 2006, **79**(2), 270–275, DOI: 10.1246/bcsj.79.270.

19 Y. Hu, Y. Zhang, C. Li, L. Wang, Y. Du and G. Mo, *et al.*, Guided Assembly of Microporous/Mesoporous Manganese Phosphates by Bifunctional Organophosphonic Acid Etching and Templating, *Adv. Mater.*, 2019, **31**(25), 1–8, DOI: 10.1002/adma.201901124, PubMed PMID: 31062894.

20 B. Boonchom, S. Youngme, S. Maensiri and C. Danvirutai, Nanocrystalline serrabrancaite ($MnPO_4{\cdot}H_2O$) prepared by a simple precipitation route at low temperature, *J. Alloys Compd.*, 2008, **454**(1–2), 78–82, DOI: 10.1016/j.jallcom.2006.12.064.

21 S. Yang, X. Li, Y. Li, Y. Wang, X. Jin and L. Qin, *et al.*, Effect of Proton Transfer on Electrocatalytic Water Oxidation by Manganese Phosphates, *Angew. Chem., Int. Ed.*, 2023, **62**(1), e202215594, DOI: 10.1002/anie.202215594, PubMed PMID: 36342503.

22 S. Yang, K. Yue, X. Liu, S. Li, H. Zheng and Y. Yan, *et al.*, Electrocatalytic water oxidation with manganese phosphates, *Nat. Commun.*, 2024, **15**(1), 1410, DOI: 10.1038/s41467-024-45705-1, PubMed PMID: 38360868.

23 J. Yang, T. Yu, X. Jiang, X. Zhang, J. Guo and Y. Chen, *et al.*, Hydrated manganese hydrogen phosphate coated membrane with excellent anticrude oil-fouling property for separating crude oil from diverse wastewater, *Surf. Coat. Technol.*, 2023, 454, DOI: 10.1016/j.surfcoat.2022.129215.

24 S. Munkaila, R. Dahal, M. Kokayi, T. Jackson and B. P. Bastakoti, Hollow Structured Transition Metal Phosphates and Their Applications, *Chem. Rec.*, 2022, **22**(8), e202200084, DOI: 10.1002/tcr.202200084, PubMed PMID: 35815949.

25 A. Bouddouch, E. Amaterz, R. Haounati, Y. Naciri, A. Taoufyq and B. Bakiz, *et al.*, Synthesis, characterization and luminescence properties of manganese phosphate $Mn_3(PO_4)_2$, *Mater. Today: Proc.*, 2020, 16–21, DOI: 10.1016/j.matpr.2019.08.058.

26 J. Cherusseri, S. A. Thomas, A. K. Pandey, M. A. Zaed, N. K. Farhana and R. Saidur, Rapid synthesis of cobalt manganese phosphate by microwave-assisted hydrothermal method and application as positrode material in supercapatteries, *Sci. Rep.*, 2024, **14**(1), 1–18, DOI: 10.1038/s41598-024-77278-w, PubMed PMID: 39489744.

27 S. H. Jhung, J. S. Chang, J. W. Yoon, J. M. Grenèche, G. Férey and A. K. Cheetham, Synthesis of transition-metal-incorporated nickel phosphate molecular sieves TMI-VSB-1, *Chem. Mater.*, 2004, **16**(26), 5552–5555, DOI: 10.1021/cm049081e.

28 J. Zhao, Q. Jing, T. Zhou, X. Zhang, W. Li and H. Pang, Controllable Synthesis of Manganese Organic Phosphate with Different Morphologies and Their Derivatives for Supercapacitors, *Molecules*, 2024, **29**(17), 4186, DOI: 10.3390/molecules29174186, PubMed PMID: 39275034.

29 Y. Zhang, Y. Liu, S. Fu, F. Guo and Y. Qian, Hydrothermally controlled growth of $MnPO_4{\cdot}H_2O$ single-crystal rods, *Bull. Chem. Soc. Jpn.*, 2006, **79**(2), 270–275, DOI: 10.1246/bcsj.79.270.

30 H. Uchiyama, I. Okumura, S. Inoue, M. Kato and M. Wakahara, Aqueous Synthesis of Manganese Phosphate Hydrate Crystals for Creating Inorganic Pigment Materials, *Inorg. Chem.*, 2021, **60**(19), 14779–14785, DOI: 10.1021/acs.inorgchem.1c02008, PubMed PMID: 34553908.

31 M. A. G. Aranda and S. Bruque, Characterization of manganese(III) orthophosphate hydrate, *Inorg. Chem.*, 2002, **29**(7), 1334–1337, DOI: 10.1021/IC00332A009.

32 G. Herzberg and L. C. Bryce, Infrared and Raman Spectra of Polyatomic Molecules, *J. Phys. Chem.*, 2002, **50**(3), 288, DOI: 10.1021/J150447A021.

33 M. Tsuboi, Vibrational Spectra of Phosphite and Hypophosphite Anions, and the Characteristic Frequencies of PO_3- and PO_2- Groups, *J. Am. Chem. Soc.*, 2002, **79**(6), 1351–1354, DOI: 10.1021/JA01563A026.

34 Y. Huang, N. A. Chernova, Q. Yin, Q. Wang, N. F. Quackenbush and M. Leskes, *et al.*, What Happens to $LiMnPO_4$ upon Chemical Delithiation?, *Inorg. Chem.*, 2016, **55**(9), 4335–4343, DOI: 10.1021/acs.inorgchem.6b00089.

35 Y. Song, J. Jiang, J. Ma, S. Y. Pang, C. Luo and W. Qin, Oxidation of inorganic compounds by aqueous permanganate: Kinetics and initial electron transfer steps, *Sep. Purif. Technol.*, 2017, **183**, 350–357, DOI: 10.1016/j.seppur.2017.04.015.

36 Y. Zhu, G. Hasegawa, K. Kanamori and K. Nakanishi, Comprehensive studies on phosphoric acid treatment of porous titania toward titanium phosphate and pyrophosphate monoliths with pore hierarchy and a nanostructured pore surface, *Inorg. Chem. Front.*, 2018, **5**(6), 1397–1404, DOI: 10.1039/C8QI00146D.

37 J. C. Munyemana, H. He, S. Ding, J. Yin, P. Xi and J. Xiao, Synthesis of manganese phosphate hybrid nanoflowers by collagen-templated biomineralization, *RSC Adv.*, 2018, **8**(5), 2708–2713, DOI: 10.1039/c7ra12628j.

38 B. Boonchom, S. Youngme, S. Maensiri and C. Danvirutai, Nanocrystalline serrabrancaite ($MnPO_4{\cdot}H_2O$) prepared by a simple precipitation route at low temperature, *J. Alloys Compd.*, 2008, **454**(1–2), 78–82, DOI: 10.1016/J.JALLCOM.2006.12.064.

39 J. Zhao, Q. Jing, T. Zhou, X. Zhang, W. Li and H. Pang, Controllable Synthesis of Manganese Organic Phosphate with Different Morphologies and Their Derivatives for Supercapacitors, *Molecules*, 2024, **29**(17), 4186, DOI: 10.3390/molecules29174186, PubMed PMID: 39275034.

40 H. Chevulamaddi and V. R. Kalagadda, Impressive electrochemical characteristics of freeze-dried nanosheet structured $Mn_2P_2O_7$ for affordable electrochemical capacitor, *Surf. Interfaces*, 2024, **55**, 105340, DOI: 10.1016/J.SURFIN.2024.105340.

41 H. Chevulamaddi and V. R. Kalagadda, Redox Mediator–assisted Electrochemical Behaviour of $Mn_2P_2O_7$ Nanoclusters for Symmetric Supercapacitors, *Fuel*, 2025, **398**, 135543, DOI: 10.1016/J.FUEL.2025.135543.

42 R. BoopathiRaja, S. Vadivel, M. Parthibavarman, S. Prabhu and R. Ramesh, Effect of polypyrrole incorporated sun flower like $Mn_2P_2O_7$ with lab waste tissue paper derived activated carbon for asymmetric supercapacitor applications, *Surf. Interfaces*, 2021, **26**, 101409, DOI: 10.1016/J.SURFIN.2021.101409.

43 E. A. Alabdullkarem and J. Khan, $Mn_2P_2O_7$–polyaniline hybrid composite as a promising electrode material for advanced symmetric supercapacitors, *RSC Adv.*, 2025, **15**(30), 24831–24843, DOI: 10.1039/D5RA04149J.